Journal of ELECTRONIC MATERIALS, Vol. 49, No. 4, 2020
https://doi.org/10.1007/s11664-020-07968-4

Effects of Sintering Method and $BaTiO_3$ Dopant on the Microstructure and Electric Properties of Bi $(Fe_{0.9}Al_{0.05}Yb_{0.05})$ O_3-Based Ceramics

GANG CHEN,[1,2,3] CONG JI,[1] TAO FAN,[1] JIAHUA LI,[1] CHUNLIN FU,[1,2] WEI CAI,[1,2] RONGLI GAO,[1,2] ZHENHUA WANG,[1,2] XIAOLING DENG,[1,2] and PEIGENG FAN[1,2]

1.—School of Metallurgy and Materials Engineering, Chongqing University of Science and Technology, Chongqing 401331, People's Republic of China. 2.—Chongqing Key Laboratory of Nano/Micro Composite Materials and Devices, Chongqing 401331, People's Republic of China. 3.—e-mail: cgyjxy_cqust@163.com

The $(1-x)$ Bi $(Fe_{0.9}Al_{0.05}Yb_{0.05})$ O_3–$x$$BaTiO_3$ (BFAYO-x BTO) ceramics were synthesized by microwave sintering (MWS) and conventional sintering (CS) methods. The crystal structure, surface morphology, dielectric and ferroelectric properties were investigated. XRD patterns show that BTO tetragonal and BFO rhombohedral phases coexist in both MWS and CS samples, and that the diffraction peaks of MWS samples shift to lower angles due to the larger ionic radius of Ba^{2+} compared with Bi^{3+}. The lattice constant of BFAYO-x BTO ceramics increases with the increase of BTO content. It was found that the average grain size of the MWS ceramic is much smaller than that of the CS ceramic. Dielectric measurements reveal that the dielectric loss and dielectric constant increase with BTO content increasing. The introduction of BTO into BFAYO-based ceramic contribute to the enhancement of the dielectric relaxation behavior. The P–E hysteresis loops demonstrate that the remnant polarization (P_r) and the coercive field (E_C) of the MWS samples are smaller than those of the CS samples. P_r and E_C first increase, then decrease and then increase again with the increase of BTO content. The maximum and minimum values of the remnant polarization were obtained at $x = 0.25$ and 0.3, respectively.

Key words: Microwave sintering, conventional sintering, crystal structure, microstructure, dielectric and ferroelectric properties

INTRODUCTION

As a single-phase room-temperature multiferroic material with the coexistence of ferroelectric and ferromagnetic properties, bismuth ferrite ($BiFeO_3$, or BFO hereafter) has been widely investigated due to its high Curie temperature ($T_C \sim 830°C$) and large spontaneous polarization ($P_s \sim 150\ \mu C/cm^2$).[1,2] However, the preparation of pure BFO with a single phase is very difficult owing to its small tolerance factor, t, along with its low structure stability. Many defects, including secondary phases (such as $Bi_2Fe_4O_9$) and oxygen vacancies caused by the evaporation of Bi elements and transformation from Fe^{3+} to Fe^{2+}, occur during the preparation process. This results in a high leakage current that would have adverse effects on the ferroelectric properties of BFO ceramics. Thus, its application is restricted. Therefore, it is very urgent to discover a method for reducing the leakage current and secondary phases.

It is well known that doping is an important method to decrease leakage currents and hinder the formation of impurities by substituting Bi^{3+} at the A

(Received August 20, 2019; accepted January 21, 2020;

site or Fe^{3+} at the B site of BFO ceramic.[3–6] The substitution of Al^{3+} and Yb^{3+} for Fe^{3+} at the B site can contribute to improve the structural stability owing to their unchanged valence. Meanwhile, the substitution of Fe^{3+} with Al^{3+} and Yb^{3+} can increase the insulation resistance without sacrificing the Curie temperature and deteriorating the ferroelectric and dielectric properties of BFO. This is ascribed to the high T_C and excellent ferroelectricity for $BiAlO_3$ ($T_C \sim 527°C$, $P_s \sim 76\ \mu C/cm^2$) and $BiYbO_3$ ($T_C \sim 650°C$).[7,8]

In addition, introducing an other perovskite compound with large t into the BFO lattice to form a solid solution may be another method to enhance the structural stability of BFO.[9–11] $BaTiO_3$ (BTO) is a typical perovskite-type lead-free dielectric material and its tolerance factor ($t = 1.062$) is much larger than that of BFO ($t = 0.84$).[12,13] Therefore, the addition of BTO into BFO can effectively stabilize the perovskite phase of BFO and enhance the ferroelectric properties by forming a solid solution, BFO–BTO.[14–18] Microwave sintering (MWS) belongs to volumetric heating and has the advantages of rapid heating, which can produce a small grain size and further contribute to the reduction of Bi volatilization and tp a dense microstructure. Therefore, the oxygen vacancy concentration decreases.[19,20] However, the structure and electric properties of BFO–BT-based ceramics synthesized by the MWS method have not been reported up until now. In the present work, $(1-x)$ Bi $(Fe_{0.9}Al_{0.05}Yb_{0.05})$ O_3–x $BaTiO_3$ ceramics were synthesized by the MWS and CS methods. In addition, the effects of BTO substitution and the MWS method on the structure, dielectric and ferroelectric properties of $(1-x)$ Bi $(Fe_{0.9}Al_{0.05}Yb_{0.05})$ O_3–$x$$BaTiO_3$ ceramics were investigated.

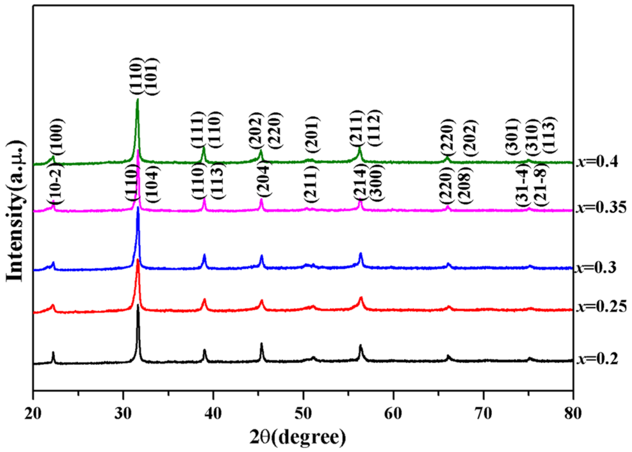

Fig. 1. XRD patterns of $(1-x)$ Bi $(Fe_{0.9}Al_{0.05}Yb_{0.05})O_3$–$x$ BTO ceramics synthesized by CS.

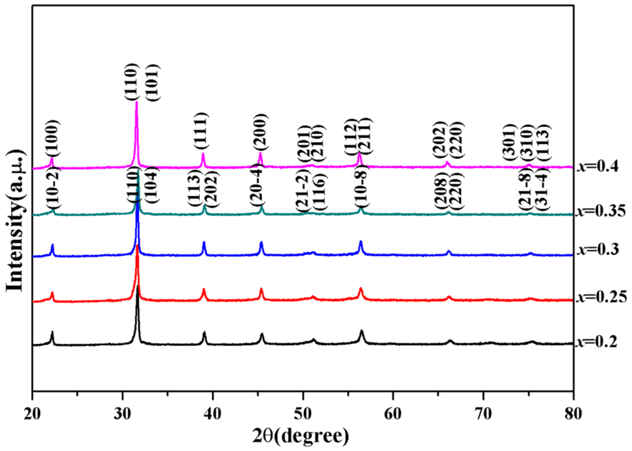

Fig. 2. XRD patterns of $(1-x)$ Bi $(Fe_{0.9}Al_{0.05}Yb_{0.05})O_3$–$x$ BTO ceramics synthesized by MWS.

MATERIALS AND METHODS

All the samples of $(1-x)$ Bi $(Fe_{0.9}Al_{0.05}Yb_{0.05})$ O_3–x $BaTiO_3$ (x = 0.2, 0.25, 0.3, 0.35 and 0.4) were synthesized by the MWS and CS techniques, respectively. The raw materials used in this experiment were titanium dioxide (TiO_2, 99%, barium carbonate ($BaCO_3$, 99%), bismuth oxide (Bi_2O_3, 99%), iron oxide (Fe_2O_3, 99%), yttrium oxide (Yb_2O_3, 99.9%) and aluminum oxide (Al_2O_3, 99%; all Aladdin). The starting materials were weighted according to stoichiometry and 5 mol.% of excess Bi_2O_3 was added to compensate for its volatilization during the sintering process. All the materials were mixed in an agate jar with distilled water and then milled for 8 h at 500 rpm in the planetary ball mill (MTR-XQM-2L'Changsha Mitr Instrument and Equipment, China). After the slurry was dried, the obtained mixtures were calcined at 820°C for 4 h with 3°C/min in a chamber furnace, and then ground again for 8 h at 500 rpm. The dried powder was granulated by mixing 6 wt.% polyvinyl alcohol (PVA) as a binder and then pressed into pellets of 10 mm in diameter and 1 mm in thickness at 15 MPa. After the PVA in the pellets was burnt off at 500°C for 8 h, the pellets were divided into two groups. Some of them were sintered at 980°C for 2 h in a conventional box furnace under an atmospheric environment for CS, and the others were sintered at the same temperature for 30 min in a microwave muffle furnace (HAMiLab–M1500; Synotherm, China) for MWS.

The phase structures of the samples were examined via x–ray diffraction (XRD;D/max 2500; Rigaku, Japan) with Cu–Kα radiation (λ = 1.541 Å) at a diffraction angle (2θ) range from 20° to 80° with an increment of 0.01° at room temperature. A scanning electron microscope (SEM; S3700; Hitachi, Japan) was used to observe the surface morphology of the ceramics.

In order to characterize the electrical properties of the $(1-x)$ Bi $(Fe_{0.9}Al_{0.05}Yb_{0.05})$ O_3–x $BaTiO_3$ ceramics, the sintered pellets were polished in an automatic grinding and polishing machine (UNIPOL-1000S; Hefei Kejing Materials Technology,

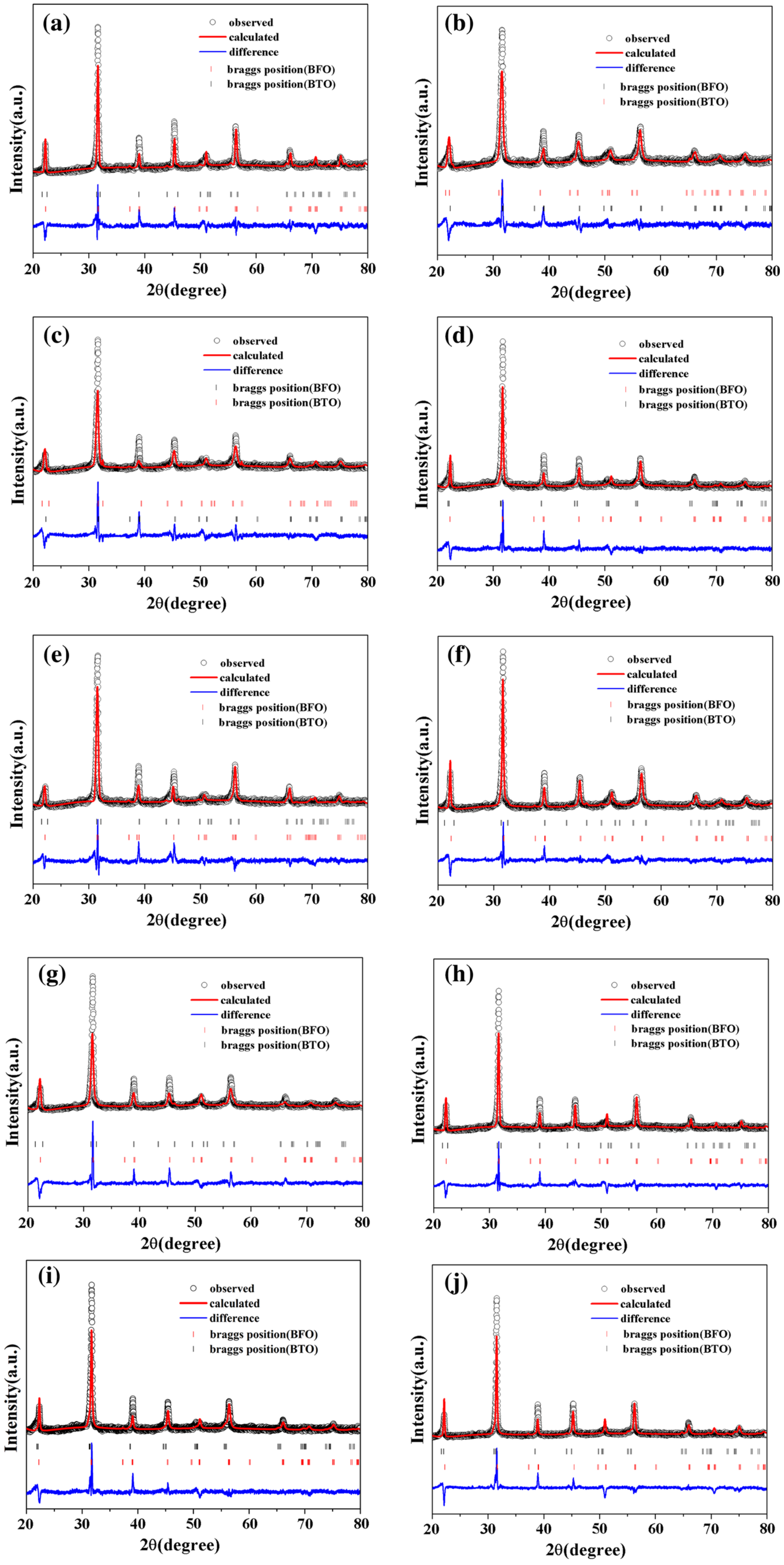

Fig. 3. Rietveld analysis of (1–x) Bi (Fe$_{0.9}$Al$_{0.05}$Yb$_{0.05}$) O$_3$–x BTO ceramics synthesized by CS and MWS: (a) x = 0.20, (b) x = 0.25, (c) x = 0.30, (d) x = 0.35 and (e) x = 0.40 for CS; (f) x = 0.20, (g) x = 0.25,(h) x = 0.30, (i) x = 0.35 and (j) x = 0.40 for MWS.

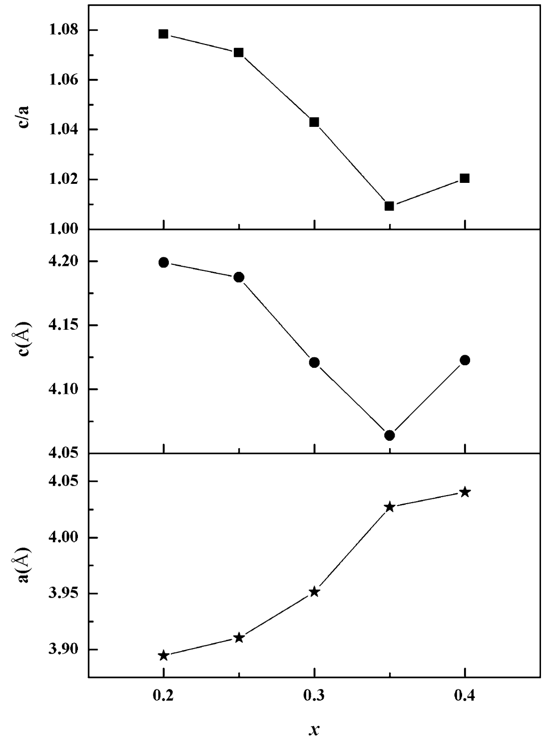

Fig. 4. Lattice constants *a* and *c* values and tetragonality *c/a* of BTO for (1 − *x*) Bi (Fe$_{0.9}$Al$_{0.05}$Yb$_{0.05}$)O$_3$–*x* BTO ceramics sintered by MWS.

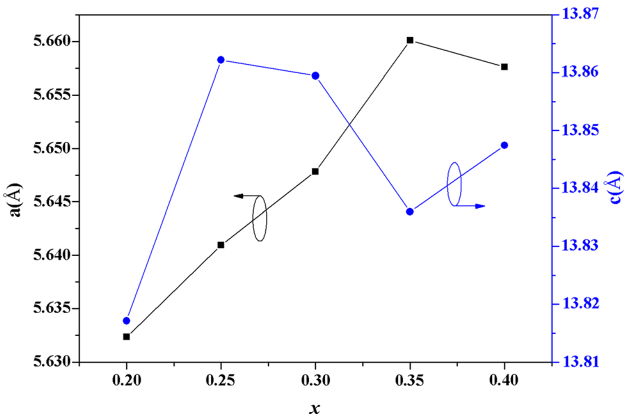

Fig. 5. Lattice constants *a* and *c* values of BFO for (1 − *x*) Bi (Fe$_{0.9}$Al$_{0.05}$Yb$_{0.05}$)O$_3$–*x* BTO ceramics sintered by MWS.

China), pasted with silver slurry on both faces, and then fired at 850°C for 30 min as electrodes. The temperature-dependence of the dielectric constant and the loss for the samples were determined by using an LCR instrument analyzer (HP4980A; Agilent, USA) within the temperature range from room temperature to 500°C. The dielectric constant (ε) can be calculated by the capacitance measured according to the following equation:

$$\varepsilon = C_t/(\varepsilon_0 A) = 4C_t/\left(\varepsilon_0 \pi d^2\right) \qquad (1)$$

where ε_0 is the dielectric constant (8.85×10^{-12} F/m) free space, C is the capacitance (F), and d and t are the diameter (m) and the thickness (m) of the samples, respectively. The ferroelectric hysteresis loops were measured by using the ferroelectric test system (TF2000; Aix–ACCT, Germany).

RESULTS AND DISCUSSION

Crystal Structure

XRD patterns of (1 − x) Bi (Fe$_{0.9}$Al$_{0.05}$Yb$_{0.05}$) O$_3$–x BTO ceramics synthesized by CS and MWS are shown in Figs. 1 and 2, respectively, in which it can be seen that all the samples present a single phase with a perovskite-type structure; no second phases are observed. At the same time, no obviously splitting peaks can be seen. In order to clarify the phases between BFO and BTO, the refinement of room-temperature x-ray diffraction analyzed by the fitting peaks method for (1 − x) Bi (Fe$_{0.9}$Al$_{0.05}$Yb$_{0.05}$)O$_3$–x BTO ceramics are shown in Fig. 3. According to the refinement results, it can be seen that the phase composition is composed of BFO with a rhombohedral phase and BTO with a tetragonal phase. This indicates that Al^{3+} and Yb^{3+} can be incorporated in the BFO lattice.

In addition, the diffraction peaks shift to the lower 2θ angle side with increasing BTO content, as shown in Figs. 1 and 2. This is mainly ascribed to the larger ionic radius of Ba^{2+} (0.135 nm) compared with Bi^{3+} (0.103 nm), while the ionic radius of Ti^{4+} (0.0605 nm) is nearly the same with Fe^{3+} (0.064 nm).[21] According to the Bragg diffraction equation:

$$2d \sin\theta = n\lambda \qquad (2)$$

where λ is the x-ray wavelength, θ is the diffraction angle, and d is the interplanar distance.

As shown in Eq. (2), it can be inferred that the larger ionic radius results in a smaller θ. As a result, the diffraction peak of the BFO ceramic should shift to the lower 2θ angle side caused by the addition of BTO into the BFO-based ceramic.

The lattice constants a and c values of BTO and BFO obtained by the structural refinement and the calculated tetragonality c/a of BTO are presented in Figs. 4 and 5, respectively. According to Fig. 4, the a value of BTO increases with the increase of BTO content, while the c and c/a of BTO increase initially and then decrease with increasing BTO content, which is consistent with the XRD analysis. As shown in Fig. 5, a value of BFO increases and then decreases with the increase of BTO content, while c value of BFO increases, then decreases and then increases with BTO content increasing.

Surface Morphology

Figure 6 shows the surface morphology of (1 − x) Bi (Fe$_{0.9}$Al$_{0.05}$Yb$_{0.05}$)O$_3$–x BTO ceramics sintered by MWS and CS. The grain sizes of the MWS samples are smaller than those of the CS samples. This is

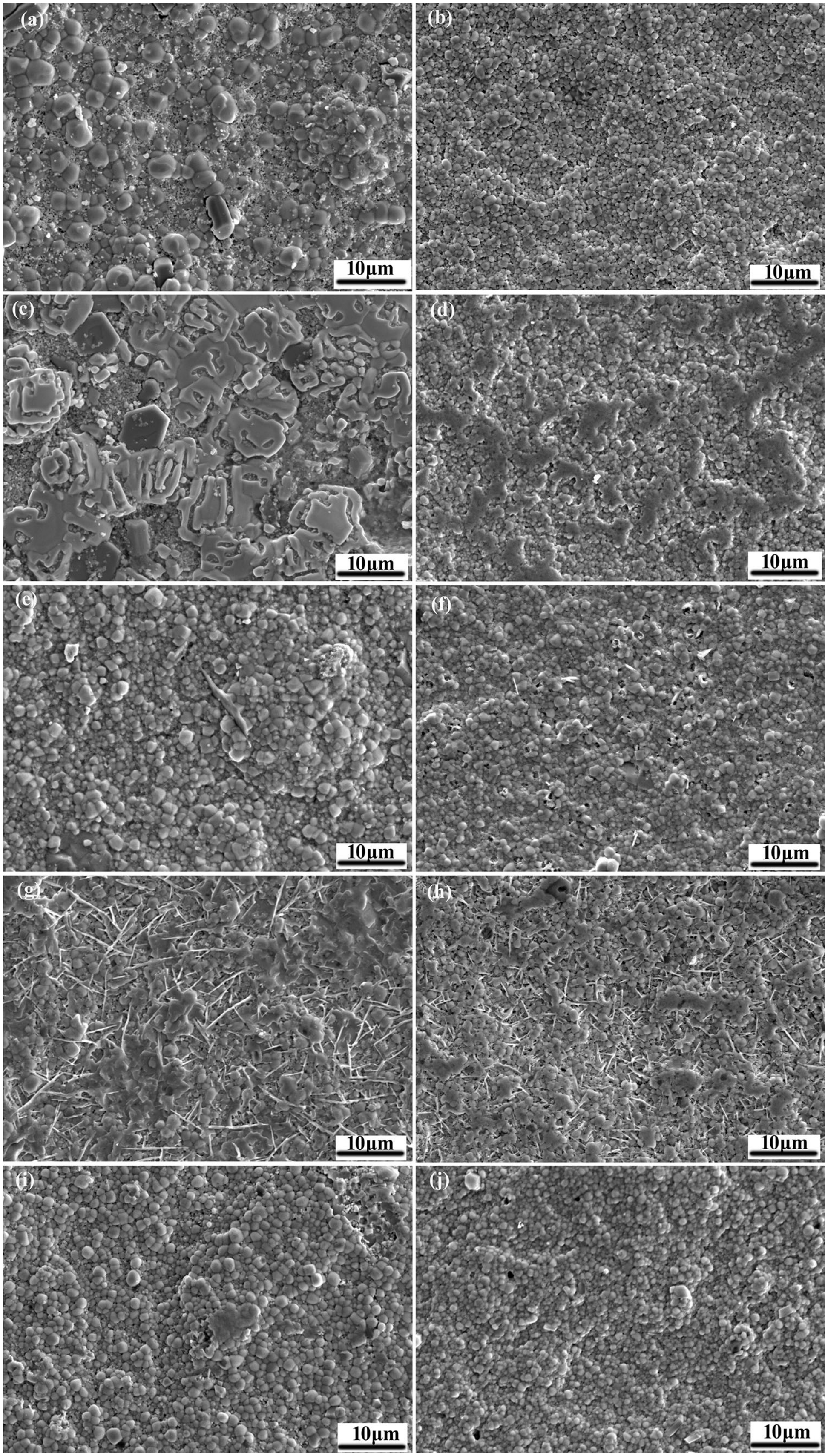

Fig. 6. SEM images of (1 − x) Bi $(Fe_{0.9}Al_{0.05}Yb_{0.05})O_3$–$x$ BTO ceramics sintered by MWS and CS: (a) $x = 0.2$, CS; (b) $x = 0.2$, MWS; (c) $x = 0.25$, CS; (d) $x = 0.25$, MWS; (e) $x = 0.3$, CS; (f) $x = 0.3$, MWS; (g) $x = 0.35$, CS; (h) $x = 0.35$, MWS; (i) $x = 0.4$, CS; (j) $x = 0.4$, MWS.

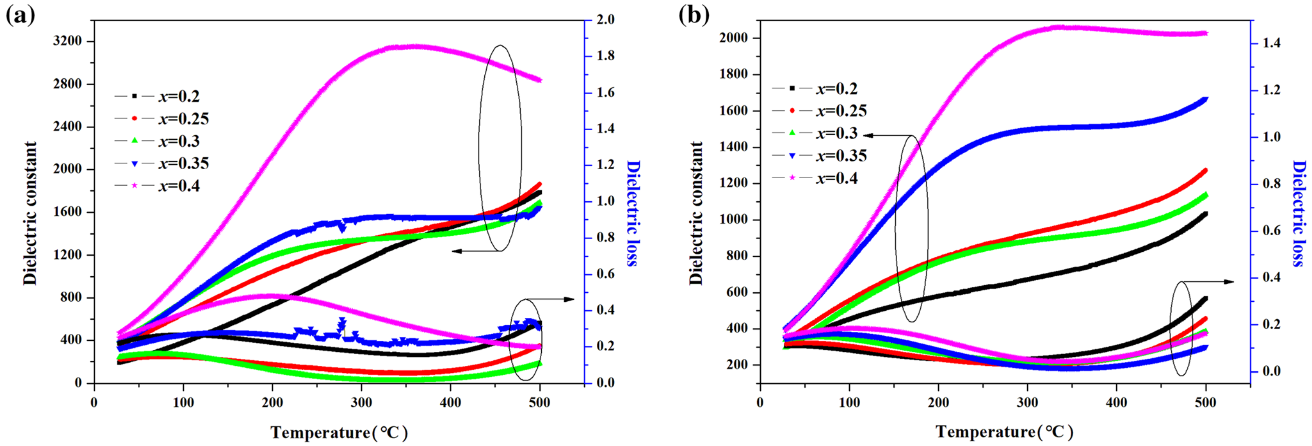

Fig. 7. The dielectric constant and dielectric loss as a function of temperature for (1 − x) Bi (Fe$_{0.9}$Al$_{0.05}$Yb$_{0.05}$)O$_3$–x BTO ceramics of CS (a) and MWS (b) at 2 MHz.

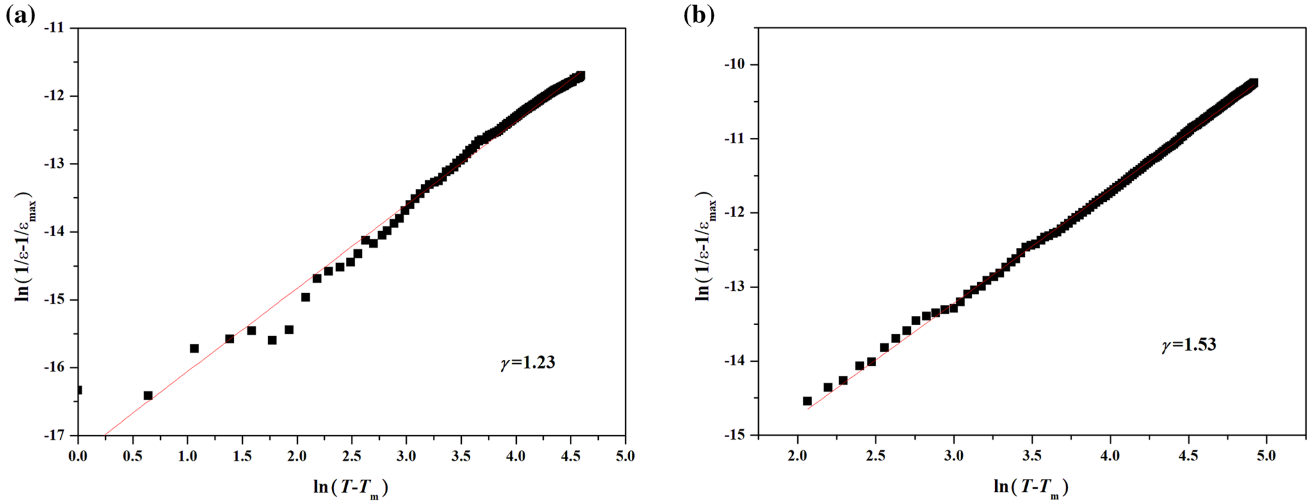

Fig. 8. ln (1/ε − 1/ε_{max}) vs ln (T − T_{max}) plot for 0.6 Bi (Fe$_{0.9}$Al$_{0.05}$Yb$_{0.05}$)O$_3$–0.4 BTO ceramics of CS (a) and MWS (b) measured at 2 MHz.

due to the rapid heating rate and thus leads to the inhibiting of the grain growth. In addition, all the samples possess relatively high densities and the grains of the MWS ceramics distribute more uniformly compared with the CS ceramics. At the same time, the grains of the CS sample with x = 0.25 growsabnormally.

Dielectric Properties

Figure 7 shows the dependence of temperature on the dielectric behavior for (1 − x) Bi (Fe$_{0.9}$Al$_{0.05}$Yb$_{0.05}$)O$_3$–x BTO ceramics synthesized by MWS and CS at 2 MHz. The values of the dielectric constants for the MWS and CS samples increase with the increase of BTO concentration. This is due to the larger dielectric constant of BTO compared with BFO.[18] At the same time, the phase transition peaks broaden for MWS ceramics compared with CS ceramics, indicating that the degree of the dielectric relaxation behavior can be strengthened by using the MWS method. The dielectric relaxation behavior can be described by using the modified Curie–Weiss law as follows:

$$\frac{1}{\varepsilon}-\frac{1}{\varepsilon_{\mathrm{m}}}=\frac{(T-T_{\mathrm{m}})^{\gamma}}{C} \qquad (3)$$

where ε and ε_{m} are the relative permittivity and the maximum permittivity, respectively, T and T_{m} are the temperature of ε and ε_{m}, respectively, γ represents the diffusion coefficient (γ = 1 for normal ferroelectric and γ = 2 for ideal relaxor ferroelectric) ,and C is the Curie constant.

The γ of 0.6 Bi (Fe$_{0.9}$Al$_{0.05}$Yb$_{0.05}$)O$_3$–0.4 BTO ceramics for CS and MWS is shown in Fig. 8, from which it can be seen that the γ of the CS sample is smaller than that of the MWS sample for 0.6 Bi

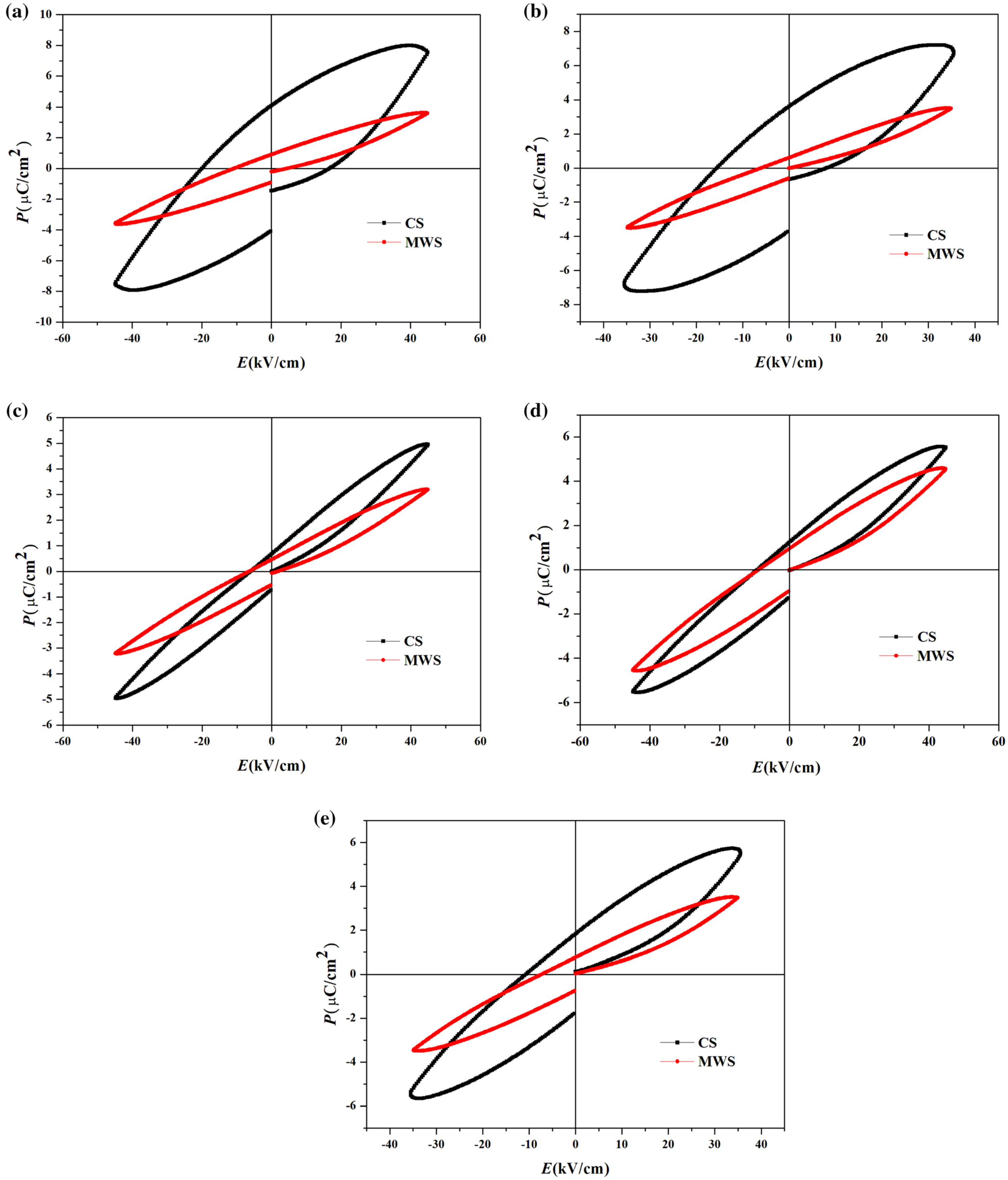

Fig. 9. *P*–*E* hysteresis loops of (1 − *x*) Bi $(Fe_{0.9}Al_{0.05}Yb_{0.05})O_3$–*x* BTO ceramics synthesized by CS and MWS methods: (a) $x = 0.2$; (b) $x = 0.25$; (c) $x = 0.3$; (d) $x = 0.35$; (e) $x = 0.4$.

$(Fe_{0.9}Al_{0.05}Yb_{0.05})O_3$–0.4 BTO. The dielectric relaxation behavior is related to the grain size. The smaller grains result in the higher dielectric relaxation behavior owing to the larger internal stress caused by the lattice distortion, as reported by Tang.[22] The addition of BTO into BFO leads to higher dielectric loss for the CS and MWS ceramics, and the dielectric loss increases with an increase of

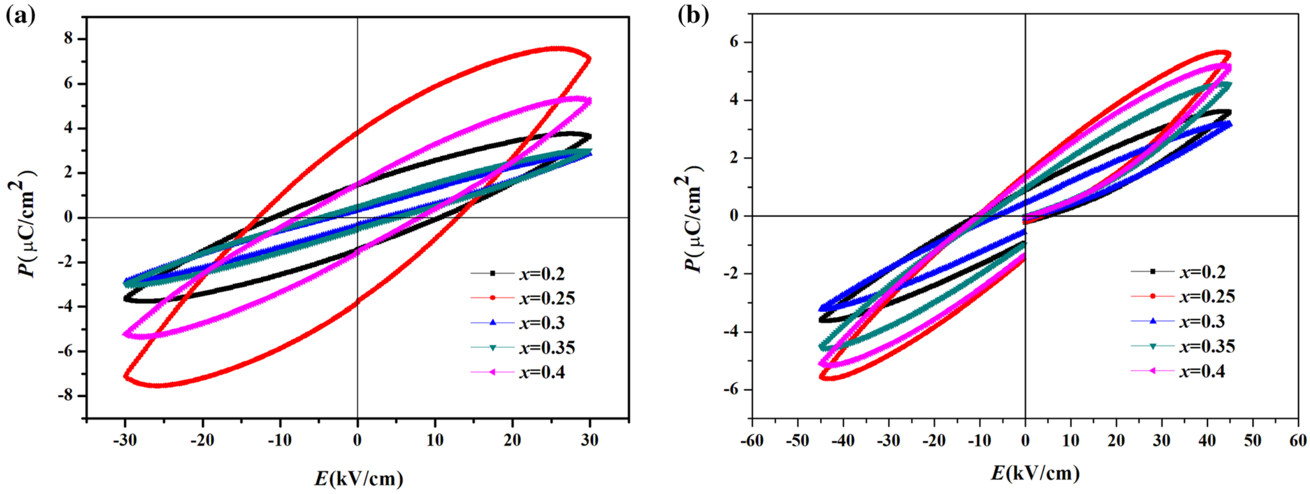

Fig. 10. P–E hysteresis loops of $(1-x)$ Bi (Fe$_{0.9}$Al$_{0.05}$Yb$_{0.05}$)O$_3$–x BTO ceramics measured at 100 Hz and 30 kV/cm for CS (a), 45 kV/cm for MWS (b).

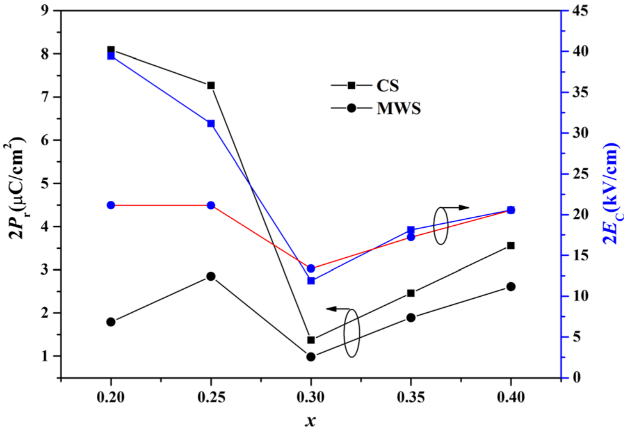

Fig. 11. P_r and E_c of $(1-x)$ Bi (Fe$_{0.9}$Al$_{0.05}$Yb$_{0.05}$)O$_3$–x BTO ceramics measured at 100 Hz and 30 kV/cm for CS, and at 45 kV/cm for MWS.

x when the temperature is relatively low. This result is consistent with Zhang's reports.[23] This phenomenon may be related to the phase transition temperature.[23,24] It has been reported that the maximum dielectric loss occurs at the phase transition temperature which shifts to a higher temperature caused by introducing BTO into the BFO ceramic.[23] Therefore, the dielectric loss of $(1-x)$ Bi (Fe$_{0.9}$Al$_{0.05}$Yb$_{0.05}$)O$_3$–x BTO ceramics increases with increasing BTO content below the phase transition temperature.

Ferroelectric Properties

Figure 9 describes the P–E hysteresis loops of $(1-x)$ Bi (Fe$_{0.9}$Al$_{0.05}$Yb$_{0.05}$)O$_3$–x BTO ceramics synthesized by the MWS and CS methods. The unsaturated hysteresis loops were observed in all the samples, indicating poor ferroelectric properties. This is due to the large leakage current caused by the transformation from Fe^{3+} to Fe^{2+} along with the volatilization of Bi.[25] Compared with the CS samples, the remnant polarization (P_r) of MWS ceramics is lower due to its smaller grains. It is well known that the domain size is in proportion to the grain size and that the domain switches are related to the domain size.[26] The smaller grain size and the smaller domain size result in more difficulty of domain switching.[27] Therefore, the P_r of the MWS samples decreases and P–E hysteresis loops become slim as compared to the CS samples. In addition, the slimmer P–E hysteresis loops of the MWS samples suggest that the dielectric loss and the leakage current become lower compared with the CS samples.[28]

In order to compare and analyze the ferroelectric properties of CS and MWS ceramics, the P–E hysteresis loops with different BTO dopant contents synthesized by the same sintering method are shown in Fig. 10. For the CS samples, P_r and the coercive field (E_C) increase, then decrease and then increase again with increasing BTO content. The largest values of P_r (3.84 μC/cm^2) and E_c (7.12 kV/cm) are obtained at $x = 0.25$, while the smallest values of P_r (0.36 μC/cm^2) and E_C (3.71 kV/cm) are obtained at $x = 0.3$, respectively. The changing trend of P_r for the MWS ceramics is the same as for the CS ceramics, and P_{rmax}(1.45 μC/cm^2) is obtained at $x = 0.25$, while the E_C values of the MWS ceramics decrease and then increase with increasing BTO content. The E_{cmax} (4.61 kV/cm) and E_{cmin} (0.61 kV/cm) are obtained at $x = 0$ and 0.35, respectively. The P_r of (1–x) Bi (Fe$_{0.9}$Al$_{0.05}$Yb$_{0.05}$)O$_3$–x BTO ceramics is also affected by oxygen vacancies. It is well known that oxygen vacancies have a pinning effect on the domain. A smaller oxygen vacancy concentration makes the domain pinning effect in ferroelectrics weaker and the domain switches easier so that P_r increases.[25] The introduction of BTO into the BFO lattice is helpful in the reduction of oxygen vacancies and so P_r increases. However, the largest value of P_r can be obtained at $x = 0.25$, which may be due to its abnormal large grain growth, and the smallest value of P_r is obtained at $x = 0.3$, which is related to the smallest grain size. The dependence of P_r and E_c values of the BTO content for $(1-x)$ Bi $(Fe_{0.9}Al_{0.05}Yb_{0.05})O_3$–$x$ BTO ceramics measured at 100 Hz are summarized in Fig. 11.

CONCLUSIONS

$(1-x)$ Bi $(Fe_{0.9}Al_{0.05}Yb_{0.05})O_3$–$x$ BTO ceramics were synthesized by using the MWS and CS methods, respectively. The structure, dielectric and ferroelectric properties were investigated systematically. BTO tetragonal and BFO rhombohedral phases coexist in both MWS and CS samples. The grain size of the MWS ceramic is smaller and distributes more uniformly than that of the CS ceramic due to the rapid heating rate of MWS. The results indicate that the MWS method contributes to the enhancement of the dielectric relaxation behavior, while the reduction of the remnant polarization is due to the slim P–E hysteresis loops. The remnant polarization increases, then decreases and then increases again with increasing BTO content. The largest remnant polarization is obtained at $x = 0.25$ for the MWS and CS samples. Its values are 3.84 $\mu C/cm^2$ for the CS ceramic and 1.45 $\mu C/cm^2$ for the MWS ceramic. Our results indicate that the MWS technique is an effective method to refine the grains and obtain the slim P–E hysteresis loops. As a result, the MWS technique can be applied in the field of the dielectric energy storage.

ACKNOWLEDGMENTS

This work was supported by the Chongqing research program of basic research and frontier technology (CSTC2019jcyj-msxmX0071, CSCT2018jcyjAX0416), the program for innovation teams in the University of Chongqing, China (CXTDX201601032), Research foundation of education bureau of Chongqing, China (KJQN201801509), the leading talents of scientific and technological innovation in Chongqing (CSTCCXLJRC201919), the excellent talent project in university of Chongqing (2017-35),the Innovation Program for Chongqing's Overseas Returnees(cx2019159) and the postgraduate science and technology innovation project of Chongqing University of Science and Technology(YKJCX1920214).

REFERENCES

1. J. Wu, Z. Fan, D. Xiao, J. Zhu, and J. Wang, *Prog. Mater Sci.* 84, 335–402 (2016).
2. G. Chen, X. Peng, C. Fu, W. Cai, R. Gao, P. Fan, X. Yi, H. Yang, C. Ji, and H. Yong, *Ceram. Int.* 44, 16880–16889 (2018).
3. R. Das, S. Sharma, and K. Mandal, *J. Magn. Magn. Mater.* 401, 29–137 (2016).
4. A. Jawad, A.S. Ahmed, S.S.Z. Ashraf, M. Chaman, and A. Azam, *J. Alloy. Compd.* 530, 63–70 (2012).
5. M. Yadav, A. Agarwal, S. Sanghi, R.K. Kotnala, J. Shah, T. Bhasin, M. Tuteja, and J. Singh, *J. Alloy. Compd.* 750, 848–856 (2018).
6. J.H. Zhu, J.Q. Dai, J.W. Xu, and X.Y. Li, *Ceram. Int.* 44, 9215–9220 (2018).
7. G. Chen, T. Fan, H. Yang, C. Fu, R. Gao, X. Deng, Z. Wang, P. Fan, and W. Cai, *Appl. Phys. A Mater.* 125, 433 (2019).
8. Z. Shen, X. Wang, B. Luo, and L. Li, *J. Mater. Chem. A.* 3, 18146–18153 (2015).
9. T. Zheng and J.G. Wu, *J. Alloy. Compd.* 676, 505–512 (2016).
10. J. Yi, Y. Tian, L.L. Wei, J.W. Li, P.F. Liang, P.P. Shi, X.L. Chao, and Z.P. Yang, *Mater. Res. Bull.* 66, 132–139 (2015).
11. J.G. Fisher, M.G. Kim, D. Kim, S.J. Cha, H.V. Vu, D. Nguyen, Y.H. Kim, S.H. Moon, and J.S. Lee, *J. Korean. Phys. Soc.* 66, 1426–1438 (2015).
12. G. Schileo, A. Feteira, K. Reichmann, M. Li, and D.C. Sinclair, *J. Eur. Ceram. Soc.* 35, 2479–2488 (2015).
13. R. Xiao, T. Hua, X. Yuan, J. Zhou, X. Ma, and D. Fu, *RSC. Adv.* 820, 12060–12068 (2018).
14. M. Tian, L. Zhou, X. Zou, Q. Zheng, L. Luo, N. Jiang, and D. Lin, *J. Mater. Sci. Mater. Electron.* 26, 8840–8847 (2015).
15. F.P. Gheorghiu, A. Ianculescu, P. Postolache, N. Lupu, M. Dobromir, D. Luca, and L. Mitoseriu, *J. Alloy. Compd.* 506, 862–867 (2010).
16. R. Das, S. Sharma, and K. Mandal, *J. Magn. Magn. Mater.* 401, 129–137 (2016).
17. A. Amouri, N. Abdelmoula, and H. Khemakhem, *J. Magn. Magn. Mater.* 417, 302–312 (2016).
18. H. Singh, A. Kumar, and K.L. Yadav, *Mater. Sci. Eng. B* 176, 540–547 (2011).
19. G. Chen, X. Peng, C. Fu, W. Cai, R. Gao, P. Fan, X. Zhang, X. Yi, C. Ji, H. Yang, and H. Yong, *J. Mater. Sci. Mater. Electron.* 29, 20017–20032 (2018).
20. V.R. Reddy, D. Kothari, S.K. Upadhyay, A. Gupta, N. Chauhan, and A.M. Awasthi, *Ceram. Int.* 40, 4247–4250 (2014).
21. R.D. Shannon, *Acta. Cryst. A.* 32, 751–767 (1976).
22. X.G. Tang, J. Wang, X.X. Wang, and H.L.W. Chan, *Solid State Commun.* 131, 163–168 (2004).
23. H. Zhang, W. Jo, K. Wang, and K.G. Webber, *Ceram. Int.* 40, 4759–4765 (2014).
24. S.W. Zhang, H.L. Zhang, B.P. Zhang, and S. Yang, *J. Alloy. Compd.* 506, 131–135 (2010).
25. W. Cai, S. Zhong, C. Fu, G. Chen, and X. Deng, *Mater. Res. Bull.* 50, 259–267 (2014).
26. Y. Huan, X. Wang, J. Fang, and L. Li, *J. Am. Ceram. Soc.* 96, 3369–3371 (2013).
27. X. Li and J. Wang, *Smart Mater. Struct.* 26, 015013 (2017).
28. Z.Y. Gao, Y.P. Pu, M.T. Yao, Q. Jin, Y.R. Wang, and H.Y. Zheng, *Ceram. Int.* 43, S85–S91 (2017).